WAVES IN RANDOM AND COMPLEX MEDIA

https://www.tandfonline.com/journals/twrm20

Impact factor = 4.853

Accepted February 1st 2023

HOMOTOPY ANALYSIS OF MIXED CONVECTION FLOW OF A MAGNETIZED VISCOELASTIC NANOFLUID FROM A STRETCHING SURFACE IN NON-DARCY POROUS MEDIA WITH REVISED FOURIER AND FICKIAN APPROACHES

M. Nasir[1], M. Waqas[2,*], O. Anwar Bég[3] and N. Zamri[1]

[1]*Faculty of Informatics and Computing, University Sultan Zainal Abidin (Kampus Gong Badak), Kuala Terengganu, Terengganu 21300,* ***Malaysia***

[2]*NUTECH School of Applied Science and Humanities, National University of Technology, Islamabad 44000,* ***Pakistan***

[3]*Professor and Director-Multi-Physical Engineering Sciences Group, Mechanical Engineering, Salford University, School of Science, Engineering and Environment (SEE), Manchester, M54WT,* ***UK***
Emails: O.A.Beg@salford.ac.uk

**Correspondence: mw_qau88@yahoo.com (M. Waqas)*

ABSTRACT: This article addresses theoretically the mixed convection hydromagnetic flow of electrically conducting viscoelastic nanofluid from a vertical permeable stretching sheet in a non-Darcy porous medium with Cattaneo–Christov double diffusion model to evaluate the heat transfer phenomena in steady boundary layer flow on a stretchable surface. In this regard thermal and solutal hyperbolic wave relaxation effects are included for non-Fourier and non-Fickian models. Heat absorption is also included in the analysis. The Buongiorno two-component nanoscale model is adopted for simulating Brownian motion and thermophoretic body force effects. A non-Darcy drag force model is employed for the porous medium and the Reiner-Rivlin second grade model for non-Newtonian characteristics. Via appropriate dimensionless similarity variables, the non–linear dimensional partial differential conservation equations for momentum, energy and concentration with associated boundary conditions are rendered into a non–linear dimensionless ordinary differential boundary value problem. The homotopy analysis method (HAM) is utilized to solve the boundary value problem and the impact of emerging parameters including thermal relaxation parameters, non-Newtonian material parameter, Darcy permeability parameter, porous inertial parameter and Hartmann magnetic number on the momentum, heat and mass transfer characteristics are visualized graphically and in Tables. A 30th order approximation for HAM is shown to produce sufficient accuracy for the velocity and temperature fields and a 40th order estimates is adequate for the concentration field. It is observed that increasing the magnitude of (thermal and solutal relaxation parameters have the opposite effect on the thermal and concentration distributions. The novelty of the work is the simultaneous inclusion of multiple effects (non-Fourier and non-Fickian thermal relaxation hyperbolic wave models, non-Darcy drag effects and heat generation/absorption) which are relevant to rheological nanomaterials processing and also the deployment of homotopy analysis as an alternative to conventional numerical methods such as finite differences, finite elements and MATLAB solvers. The study is relevant to the manufacture of electro-conductive polymers (ECPs) and smart (functional) magnetic nano-liquids.

KEYWORDS: *Heat generation/absorption, magnetic field, non-Newtonian flow; Homotopy approach, Darcy–Forchheimer*, *Mixed convection, Cattaneo–Christov double diffusion.*

1. INTRODUCTION

Thermosolutal convection i. e. simultaneous heat and mass transfer, finds numerous applications in many industrial applications including paper production, bioreactors, crystal growth, materials processing and coating systems. Buoyancy forces frequently arise in such flows. Conventional mathematical models of heat conduction employ the Fourier law [1]. Similarly, mass diffusion (species transport) is generally simulated with the Fick law. These approaches however have limitations since they neglect thermal and concentration relaxation characteristics which can arise in technological designs and can result in erroneous predictions of temperature and concentration distributions. In the Fourier and Fickian models, both temperature profile and concentration profile are parabolic differential equations. By adding relaxation time, Cattaneo [2] generalized the Fourier model to a hyperbolic partial differential equation which capture the effect of heat waves. This non-Fourier model has resolved a number of challenging problems in thermophysics and thermal engineering analysis. Christov [3] further extended the Cattaneo model to consider material invariance (indifferent frame) and heat conduction. Many interesting studies have subsequently been communicated deploying this non-Fourier approach. Thermal convection in incompressible Newtonian fluid with the generalized non-Fourier Cattaneo–Christov model has been investigated by Straughan [4]. The non-Fickian model has also been popularized in modern species diffusion analysis and has served to enable more sophisticated simulations of mass transfer in technological processes. When *both non-Fourier and non-Fickian approaches are combined*, then generalized thermosolutal models can be developed. The resulting boundary value problems for viscous flows with heat and mass transfer are important in materials processing operations and are strongly nonlinear and generally require very robust numerical or semi-numerical/analytical methods for their solution. Hayat *et al*. [5] implemented Liao's homotopy analysis technique which uses an embedding parameter for accelerated convergence, to simulate the effects of Cattaneo–Christov double–diffusion, chemical reaction and heat source/sink on Walters'–B viscoelastic nanofluid flow from a stretching surface. Hayat *et al.* [6] further studied the dynamics of a second–grade viscoelastic nanofluid from a stretching plane with Cattaneo–Christov double diffusion. These studies showed that local Nusselt number (wall heat transfer rate) is elevated with non-Fourier thermal relaxation time and Sherwood number (wall mass transfer rate) is enhanced with non-Fickian solutal relaxation time.

Yu Bai *et al.* [7] used a novel double-parameter transformation expansion method with the base function method (DPTEM-BF) to compute the Cattaneo–Christov double diffusive magnetized reactive stagnation point flow of a viscoelastic Oldroyd–B nanofluid from a stretching surface with thermal radiation flux. They noted that increasing thermal relaxation and solutal relaxation parameters elevate thermal and species (concentration) boundary layer thicknesses. Further studies deploying Cattaneo–Christov double diffusion include Ijaz and Ayub [8] who computed the influence of activation energy and dual stratification in nonlinear Walters-B viscoelastic convection from a permeable stretched sheet). Ibrahim and Gadisa [9] used a finite element approach for computing non-linear convective flow of Oldroyd-B non-Newtonian fluid with from a non-linear stretching sheet with heat generation or absorption. Tulu and Ibrahim [10] combined the Cattaneo–Christov heat and mass transport model with thermal conductivity variation to analyze Casson nanofluid flow external to a stretching cylinder. Rawat *et al.* [11] used Runge–Kutta–Fehlberg and shooting techniques to study numerically the Cattaneo–Christov double diffusion in Oldroyd–B convective flow from a stretching surface. All these studies confirmed that the non-Fourier and non-Fickian models produce results which diverge significantly from the classical Fourier and Fickian approaches.

In recent years a new group of functional materials have been developed which combine polymeric properties with electromagnetic smart properties. Known as *electro-conductive polymers (ECPs)* [12] such complex materials are of great interest in naval, propulsion, fuel cell and biomedical industries. The simulation of the manufacturing of such fluids requires mathematical and computational models which combine magnetohydrodynamics (MHD) with rheological fluid dynamics. Non–Newtonian models can be broadly divided into three general categories due to the shear stress-strain characteristics associated with different liquids and these are the differential form, integral form, and rate form. Magnetic polymeric fluids provide enhanced protection to engineering systems and are becoming increasingly popular for anti-corrosion coatings and also protection from other hazards. Engineers are also combining nanoscale properties with electro-conductive polymers to develop the next generation of magnetic nano-polymers [13]. The Buongiorno two-component nanoscale model is useful for simulating heat and mass transfer in such coating fluids. Magnetohydrodynamic flows of both macroscopic and nanoscale non-Newtonian functional fluids have stimulated considerable interest as they have direct relevance to enrobing, coating and surface deposition technologies in materials processing. In such systems, a transverse or radial external magnetic field is imposed to generate a Lorentzian body force which interacts with the magnetic fluid and therefore offers an excellent mechanism for controlling momentum and thermal diffusion. Kumaran *et al.* [15] deployed an optimized second order Keller finite difference scheme, Buongiorno's model and the tangent hyperbolic shear-thinning model to simulate the the boundary layer characteristics of enrobing flow of a magnetic functional nanofluid coating on a cylinder with chemical reaction, gyrotactic bioconvection and non-Fourier relaxation effects. Umavathi *et al.* [16] used MATLAB quadrature to compute the time-dependent squeezing flow, heat and mass transfer in a magnetic nanofluid with mixed boundary conditions as a model of smart lubrication. Abbas *et al.* [17] employed neural networks and second law thermodynamics to analyze the peristaltic pumping of magnetic Williamson non-Newtonian nanofluid in a deformable vessel. Several investigators have also considered Cattaneo-Christov double diffusion effects in magnetic non-Newtonian nanofluid transport. Hayat *et al.* [18] used the homotopy analysis method to study thermal and solutal relaxation effects with entropy generation in magnetic viscoelastic nanofluid flow along a Riga sensor. Hafeez *et al.* [19] studied the swirling flow of a magnetic Oldroyd-B elastic-viscous nanofluid with Cattaneo-Christov double diffusion from a rotating disk. They observed that increment in non-Fourier thermal and non-Fickian solutal relaxation time parameters result in a depletion in temperature and concentration values. They further showed that axial flow is decelerated with greater viscoelastic retardation time parameter, whereas greater nanofluid thermophoretic body force elevates temperatures. Ijaz *et al*. [20] studied the effects of Arrhenius activation energy, Joule magnetic heating, binary chemical reaction, dual stratification and Cattaneo–Christov double-diffusion on convective flow of a Walters-B nanofluid over a stretching sheet. They noted that heat transfer rate is enhanced with larger thermal relaxation parameter, whereas greater thermal and solutal relaxation parameters decrease both temperature and concentration fields.

In many materials fabrication processes e.g. coating, porous media [21] are exploited since they offer an inexpensive filtration medium which can be used to regulate transport characteristics of completed products. A porous medium comprises solid matrix fibres with interconnected pores, to constitute a matrix structure. In boundary layer models of flow through porous media, which are appropriate for coating simulations, macroscopic models can be used and the most popular are the Darcy model law and Kozeny-Carman model, both of which are generally valid at low Reynolds numbers (viscous dominated flows). The advantage of such models is that they can be easily accommodated in the framework of boundary layer theory and do not require morphological data to characterize the porous medium. They instead utilize a permeability (and also porosity) to describe the hydraulic conductivity of the medium. The simplicity of such models provides a reasonable estimate of the overall flow behavior in the porous media but cannot furnish details of the microscale flow field [22]. Several investigations have reported on the transport of magnetic functional liquids in Darcian porous media, for which the permeability is assumed to be isotropic. Shamshuddin *et al*. [23] analyzed thermocapillary magnetohydrodynamic convection in Copper-water based nanofluid flow from a disk in Darcian porous media with radiative flux. Bhatti *et al.* [24] studied cross diffusion, hydrodynamic and thermal slip effects on magnetic Fe_3O_4-water-based nanofluid transport from a nonlinear stretching sheet in Darcian porous media. Shamshuddin *et al.* [25] used the Adomian decomposition method (ADM) to compute the magnetized radiative-convective non-Newtonian (Sisko) fluid flow over a bi-directional stretching sheet in a porous medium with homogeneous–heterogeneous reactions. In porous media, at higher Reynolds numbers, inertial drag effects can also be generated. These are usually simulated with the Darcy-Forchheimer drag force model in which an additional second order Forchheimer drag force term is deployed. This model has emerged as very versatile in numerous areas of fluid mechanics including Taylor dispersion in blood coagulation flows in tissue [26] and coating of curved bodies with magneto-rheological liquids [27]. Revathi *et al.* [27] investigated the transient mixed convective nanofluid flow with an exponentially decreasing free-stream velocity distribution in non-Darcy porous medium. Khan *et al.* [28] used Mathematica software to simulate the effects of activation energy on magnetohydrodynamic mixed convection in Darcy-Forchheimer stagnation flow of Carreau nanofluid with thermal radiation. Umavathi *et al.* [30] investigated the effects of convective wall boundary conditions on reactive mixed convection in Darcy-Forchheimer porous media. Several articles have also addressed the impact of with Cattaneo–Christov double diffusion in Darcy-Forchheimer porous media boundary layer convection flows. Muhammad *et al.* [31] examined the Darcy–Forchheimer flow over an exponentially stretching curved surface with Cattaneo–Christov double diffusion using the NDSolve method. They showed that heat and mass transfer rates are elevated with increment in non-Fourier thermal and non-Fickian concentration relaxation parameters. Nayak *et al.* [32] studied entropy generation and Cattaneo-Christov double-diffusion in hybrid viscoplastic nanofluid transport in Darcy-Forchheimer porous media from a curved surface with the bvp4c scheme in MATLAB. They showed that temperatures are boosted with greater curvature parameter and Forchheimer number whereas concentration magnitudes are enhanced with Darcy parameter.

The focus of the present study is to simulate, as a model for industrial magnetic polymeric coating, the *mixed convection hydromagnetic flow of electrically conducting viscoelastic nanofluid from a vertical permeable stretching sheet in a non-Darcy porous medium with the Cattaneo–Christov double diffusion model (thermal and solutal relaxation effects).* Heat absorption is also included in the analysis. The Buongiorno two-component nanoscale model is adopted for simulating Brownian motion and thermophoretic body force effects. The Darcy-Forchheimer drag force model is employed for the porous medium and the Reiner-Rivlin differential second grade model for non-Newtonian characteristics (relaxation and retardation). Via appropriate dimensionless similarity variables, the non–linear dimensional partial differential conservation equations for momentum, energy and concentration with associated boundary conditions are transformed into a non–linear dimensionless ordinary differential boundary value problem. The homotopy analysis method (HAM) [33] is utilized to solve the boundary value problem and the impact of emerging parameters including thermal relaxation parameters, non-Newtonian material parameter, Darcy permeability parameter, porous inertial (Forchheimer) parameter and modified Hartmann magnetic number on the momentum, heat and mass transfer characteristics are visualized graphically and in Tables. The *novelty of the present study is the simultaneous consideration of non-Fourier and non-Fickian effects, magnetohydrodynamics, viscoelastic characteristics and also heat source/sink*. The current study is relevant to the fabrication of the electroconductive nano-polymers in industrial coating flows.

2.MATHEMATICAL MODEL

Consider the two-dimensional, steady-state thermosolutal convection flow of a magnetized viscoelastic (second grade Reiner-Rivlin) nanofluid induced by a vertical permeable stretching plane adjacent to a non-Darcy porous medium, as a model of magnetic nano-polymer coating processing. The physical model is depicted in **Fig. 1**. A transverse static magnetic field is applied. Hall and ionslip effects are neglected as is Ohmic dissipation. The non-Fourier and non-Fickian Cattaneo–Christov double–diffusion model is employed [18-20]. The fluid emerges at $y = 0$ and is constrained within the range $y \geq 0$. The non-Fourier and non-Fickian Cattaneo–Christov double-diffusion model is implemented to describe thermal relaxation and solutal relaxation effects. Heat generation/absorption is also considered.

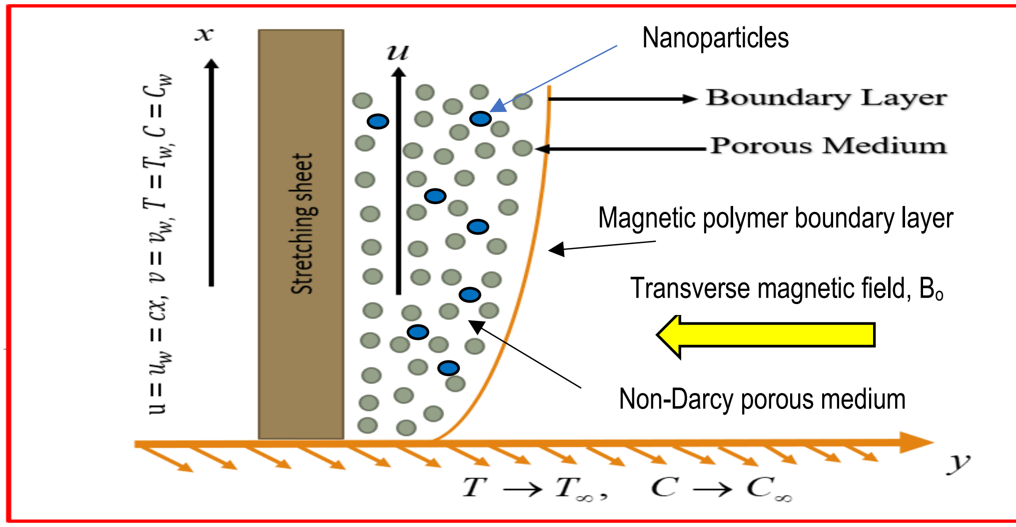

Fig.1. Physical image of the flow.

Buongiorno's nanofluid model [14] is employed which allows the inclusion of a nanoparticle species diffusion equation, and the contributions of thermophoresis and Brownian motion. Both thermal and nanoparticle species (solutal) buoyancy are included. The permeable sheet permits suction and injection. The stretching sheet velocity is defined by $u_w(x) = cx$, where c is a dimensional constant. Under the boundary layer and Boussineq approximations, the appropriate conservation equations for *second grade viscoelastic Buongiorno nanofluid thermo-magneto flow* i. e. mass, momentum, energy and species concentration may be expressed extending the models in [6], [18] and [20] as:

$$\frac{\partial u}{\partial x} + \frac{\partial v}{\partial y} = 0, \tag{1}$$

$$\begin{cases} u\dfrac{\partial u}{\partial x} + v\dfrac{\partial v}{\partial y} = v\dfrac{\partial^2 u}{\partial y^2} + \dfrac{\alpha_1}{\rho_f}\left(u\dfrac{\partial^3 u}{\partial x \partial y} + \dfrac{\partial u}{\partial x}\dfrac{\partial^2 u}{\partial y^2} + v\dfrac{\partial^3 u}{\partial y^3} - \dfrac{\partial u}{\partial y}\dfrac{\partial^2 u}{\partial x \partial y}\right) \\ -\dfrac{v}{K^*}u - Fu^2 - \dfrac{\sigma B_0^2}{\rho_f}u + g\big(\beta_T(T - T_\infty) + \beta_C(C - C_\infty)\big) \end{cases}, \tag{2}$$

$$\begin{cases} u\frac{\partial T}{\partial x}+v\frac{\partial T}{\partial y}=\alpha\frac{\partial^2 T}{\partial y^2}-\lambda_t\begin{bmatrix}\frac{\partial T}{\partial x}\left(u\frac{\partial u}{\partial x}+v\frac{\partial u}{\partial y}\right)+\frac{\partial T}{\partial y}\left(u\frac{\partial v}{\partial x}+v\frac{\partial v}{\partial y}\right)\\ +2uv\frac{\partial^2 T}{\partial x\partial y}+u^2\frac{\partial^2 T}{\partial x^2}+v^2\frac{\partial^2 T}{\partial y^2}\end{bmatrix}\\ +D_B\lambda_t\tau\left[u\frac{\partial^2 C}{\partial x\partial y}\frac{\partial T}{\partial y}+u\frac{\partial C}{\partial y}\frac{\partial^2 T}{\partial x\partial y}+v\frac{\partial^2 C}{\partial y^2}\frac{\partial T}{\partial y}+v\frac{\partial C}{\partial y}\frac{\partial^2 T}{\partial y^2}\right]\\ +2\lambda_t\tau\frac{D_T}{D_\infty}\left[u\frac{\partial T}{\partial y}\frac{\partial^2 T}{\partial x\partial y}+v\frac{\partial^2 T}{\partial y^2}\frac{\partial T}{\partial y}\right]+\frac{Q_0}{(\rho c)_f}(T-T_\infty)+\frac{Q_0}{(\rho c)_f}\lambda_t\left[u\frac{\partial T}{\partial x}+v\frac{\partial T}{\partial y}\right] \end{cases}, \tag{3}$$

$$\begin{cases} u\frac{\partial C}{\partial x}+v\frac{\partial C}{\partial y}=D_B\frac{\partial^2 C}{\partial y^2}-\lambda_c\begin{bmatrix}\frac{\partial C}{\partial x}\left(u\frac{\partial u}{\partial x}+v\frac{\partial u}{\partial y}\right)+\frac{\partial C}{\partial y}\left(u\frac{\partial v}{\partial x}+v\frac{\partial v}{\partial y}\right)\\ +2uv\frac{\partial^2 C}{\partial x\partial y}+u^2\frac{\partial^2 C}{\partial x^2}+v^2\frac{\partial^2 C}{\partial y^2}\end{bmatrix},\\ \qquad -\frac{D_T}{D_\infty}\left[u\frac{\partial^3 T}{\partial x\partial y^2}+v\frac{\partial^3 T}{\partial y^3}+\frac{\partial^2 T}{\partial y^2}\right] \end{cases} \tag{4}$$

$$u=u_w(x)=cx,\ v=-v_w,\ T=T_w,\ C=C_w \text{ at } y=0, \text{ at } y=0, \tag{5a}$$

$$u\to 0,\ T\to T_\infty,\ C\to C_\infty \text{ when } y\to\infty. \tag{5b}$$

Here $\upsilon\left(=\frac{\mu}{\rho_f}\right)$ characterizes the kinematic viscosity, ρ_f denotes the magnetic nanofluid density, μ is dynamic viscosity, g is the gravitational acceleration, F is the Forchheimer quadratic inertial porous medium coefficient, (β_T, β_C) are thermal/concentration expansion coefficients, α_1 is the viscoelastic material constant, K^* is permeability of the isotropic, homogenous porous medium, σ is electrical conductivity of the magnetic nanofluid, B_0 is magnetic field strength, $\alpha=\frac{k}{(\rho c)_f}$ is thermal diffusivity, $\tau=\frac{(\rho c)_p}{(\rho c)_f}$ denotes heat capacity ratio with $(\rho c)_f$ for liquid heat capacity and $(\rho c)_p$ for nanoparticles effective heat capacity, (D_T, D_B) are the thermophoresis and

Brownian diffusion coefficients, respectively, Q_0 is the coefficient of heat absorption/generation [6], (T, C) are magnetic nanofluid temperature and concentration, $(u_w(x), v_w)$ for (stretching, suction/injection) velocities, k is thermal conductivity of the magnetic nanofluid, c is the sheet stretching rate, (T_∞, C_∞) are ambient liquid (temperature, concentration) respectively, (T_w, C_w) are constant wall (temperature, concentration) respectively, (λ_t, λ_c) designate the relaxation times (thermal, solutal) and (u, v) are components of velocity in the (x, y) directions respectively.

Introducing the following transformations:

$$\begin{cases} \eta = y\sqrt{\dfrac{c}{\upsilon}},\ u = cxf'(\eta),\ v = -\sqrt{c\upsilon}\, f(\eta), \\ \theta(\eta) = \dfrac{T - T_\infty}{T_f - T_\infty},\ \phi(\eta) = \dfrac{C - C_\infty}{C_f - C_\infty}. \end{cases} \tag{1}$$

The mass conservation Eqn. (1) is fulfilled automatically, and the momentum, energy and nanoparticle concentration boundary layer Eqns. $(2)-(6)$ emerge as:

$$f''' + f\,f'' + K\left(2f'\,f''' - f''^2 - f\,f^{iv}\right) - \left(\lambda + Ha^2\right) f' - \left(1 + F_r\right) f'^2 + \lambda_1\left(\theta + N\phi\right) = 0, \tag{2}$$

$$\begin{aligned} &\theta'' + \Pr f\theta' + \Pr N_b\phi'\theta' + \Pr N_t\theta'^2 + \Pr S\theta + \Pr S\delta_1 f\theta' + \\ &+ \Pr \delta_1\left(-ff'\theta' - f^2\theta'' - 2N_t f\theta'\theta'' - N_b f\theta'\phi'' - N_b f\theta''\phi'\right) = 0, \end{aligned} \tag{3}$$

$$\phi'' + Scf\phi' + \frac{N_t}{N_b}\theta'' + Sc\,\delta_2\left(-ff'\phi' - f^2\phi''\right) - \delta_2\frac{N_t}{N_b} f\theta'' = 0, \tag{4}$$

The boundary conditions (7) become:

$$f = h,\ f' = 1,\ \theta = 1,\ \phi = 1 \text{ at } \eta = 0, \tag{5}$$

$$f' \to 0,\ \theta \to 0,\ \phi \to 0 \text{ as } \eta \to \infty. \tag{6}$$

Here $(')$ signifies differentiation with respect to η, K denotes second grade viscoelastic material parameter of the magnetic nanofluid, λ is the permeability (Darcy) parameter, Ha is modified Hartmann number, F_r is the local Forchheimer inertial coefficient, C_b is porous medium drag coefficient, C_b^* is porous medium drag coefficient per unit length, S is the heat source/sink parameter i.e. for heat generation $(S>0)$ and for heat absorption $(S<0)$ variable, N_t is thermophoresis variable, $\Pr$ is Prandtl number, N_b is Brownian motion variable, λ_1 is mixed convection factor, N is the ratio of concentration to thermal buoyancy forces, Gr_x is the local Grashof number (thermal buoyancy parameter), $Gr^*{}_x$ is the local solutal Grashof number (nanoparticle species concentration buoyancy parameter), Re_x is local Reynolds number, Sc is Schmidt number, (δ_1, δ_2) represent the non-Fourier and non-Fickian relaxation times (thermal, solutal), h is the wall lateral mass flux parameter i.e. for suction $(h>0)$ and injection $(h<0)$. These variables are defined as follows:

$$
\begin{aligned}
&K=\frac{\alpha_1 c}{\mu}, \lambda=\frac{\upsilon}{K^* c}, Ha=\frac{\sigma B_0^2}{c\rho_f},\ F_r=\frac{C_b x}{\sqrt{K^*}},,\ C_b=\frac{C_b^*}{x},\ \delta_1=\lambda_t c,\ \delta_2=\lambda_c c,\\
&N_t=\frac{\tau D_T\left(T_f-T_\infty\right)}{T_\infty \upsilon}, \Pr=\frac{\upsilon}{\alpha},\ N_b=\frac{\tau D_B\left(C_w-C_\infty\right)}{\upsilon}, \lambda_1=\frac{Gr_x}{\mathrm{Re}_x^2}, N=\frac{Gr_x^*}{Gr_x},\\
&\mathrm{Gr}_x\left(=\frac{g\beta_T\left(T_w-T_0\right)x^3}{\upsilon^2}\right),\quad \mathrm{Gr}_x^*\left(=\frac{g\beta_C\left(C_w-C_0\right)x^3}{\upsilon^2}\right), \mathrm{Re}_x=\frac{cx^2}{\upsilon},\\
&Sc=\frac{\upsilon}{D_B}, h=\frac{v_w}{\sqrt{c\upsilon}},\ S=\frac{Q_0}{(\rho c)_f\ c}.
\end{aligned}
\tag{7}
$$

The skin–friction coefficient at the stretching sheet (wall) may be defined as:

$$
C_{fx}=\frac{2\tau_w}{\rho u_w^2},\ \tau_w=\mu\left(\frac{\partial u}{\partial y}\right)_{y=0}+\alpha_1\left(\begin{gathered} u\frac{\partial}{\partial x}\left(\frac{\partial u}{\partial y}\right)+\left(\frac{\partial}{\partial y}\left(\frac{\partial u}{\partial y}\right)\right)\upsilon \\ +2\left(\left(\frac{\partial u}{\partial y}\right)\left(\frac{\partial u}{\partial x}\right)\right)\end{gathered}\right)_{y=0}, \tag{8}
$$

In non–dimensional variables, the appropriate expression is:

$$
C_{fx}\,\mathrm{Re}_x^{-\frac{1}{2}}=(1+3K)\,f''(0), \tag{9}
$$

3.HOMOTOPY ANALYSIS METHOD (HAM) SIMULATION

The nonlinear coupled ordinary differential boundary value problem defined by Eqns. (8)-(12) are solved by the Liao homotopy analysis method (HAM) [33]. This technique is extremely accurate and has been deployed in multiple nonlinear magnetic and non-Newtonian thermo-fluid dynamics problems. Recent applications include ionized dielectric rotating MHD generator viscous flows [34], thermal polymeric micropolar wedge coating flows [35], Hall magneto-fluid dynamics with microstructural effects [36], entropy generation in magnetic slip coating flows [37] and magnetic propulsion flows in ducts [38]. For the present problem, using HAM we make the initial guesses $\left(f_o(\eta),\, \theta_o(\eta),\, \phi_o(\eta)\right)$, and define auxiliary linear operators $\left(L_f,\, L_\theta,\, L_\phi\right)$ as follows:

$$\begin{gathered} f_0(\eta) = 1 - e^{-\eta}, \\ \theta_0(\eta) = e^{-\eta}, \\ \phi_0(\eta) = e^{-\eta}, \end{gathered} \tag{10}$$

$$\begin{cases} L_f = f''' - f', \\ L_\theta = \theta'' - \theta, \\ L_\phi = \phi'' - \phi, \end{cases} \tag{11}$$

with

$$\begin{cases} L_f\left(A_1 + A_2 e^{\eta} + A_3 e^{-\eta}\right) = 0, \\ L_\theta\left(A_4 e^{\eta} + A_5 e^{-\eta}\right) = 0, \\ L_\phi\left(A_6 e^{\eta} + A_7 e^{-\eta}\right) = 0, \end{cases} \tag{12}$$

Here $C_i\left(i = 1-7\right)$ indicate the arbitrary constants.

3.1 Convergence analysis

When deploying HAM, it is critical to achieve accelerated convergence. This method involves an auxiliary parameter h, which facilitate the selection of a convergence area of velocity $f''(0)$, temperature $\theta'(0)$, and nanoparticle concentration $\phi'(0)$. The auxiliary parameter h therefore plays a vital role. In Figs 2-3, the appropriate h–curves are visualized. It is evident that approved values of h_f, h_θ and h_ϕ in Figs. 2 and 3 are enforced over the ranges $-1.5 \le h_f \le -0.1$, $-1.5 \le h_\theta \le -0.2$ and $-1.5 \le h_\phi \le -0.3$. The convergence of velocity $f''(0)$, temperature $\theta'(0)$, and concentration $\phi'(0)$ are presented in **Table 1**. It is concluded that 30th order HAM estimate is sufficient for $f''(0)$ and $\theta'(0)$ whereas the 40th order HAM of estimates is adequate for $\phi'(0)$ respectively.

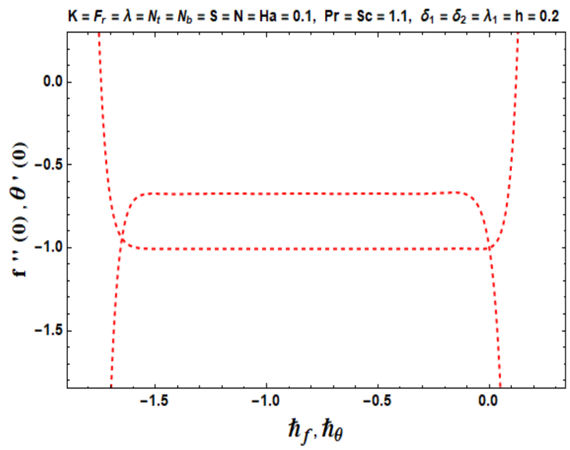

Fig. 2. H– curve influence for $f''(0),\theta'(0)$.

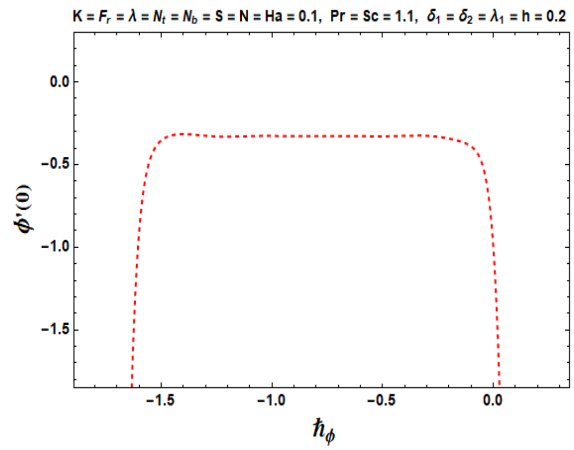

Fig. 3. H–curve influence for $\phi'(0)$.

Table 1. Convergence of HAM resolutions while $Ha = K = N_t = N_b = N = \lambda = F_r = S = 0.1,$

$\Pr = Sc = 1.1, \quad \delta_1 = \delta_2 = \lambda_1 = h = 0.2$.

Oder of HAM approximations	$-f''(0)$	$-\theta'(0)$	$-\phi'(0)$
1	-1.0119	-0.7803	-0.5089
10	-1.0075	-0.6744	-0.3257
20	-1.0072	-0.6732	-0.3290
30	-1.0073	-0.6737	-0.3270
40	-1.0073	-0.6737	-0.3274
50	-1.0073	-0.6737	-0.3274

4.RESULTS AND DISCUSSION

Extensive computations of the HAM solutions have been conducted in symbolic software and all graphical visualizations for the influence of the emerging key physical parameters on the velocity $f'(\eta)$, temperature $\theta(\eta)$ and concentration $\phi(\eta)$ profiles and additionally the skin friction are shown in **Figs. 4-22**.

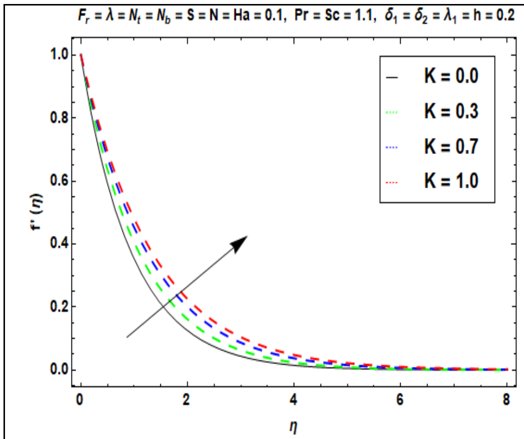

Fig. 4. Impact of $f'(\eta)$ via K.

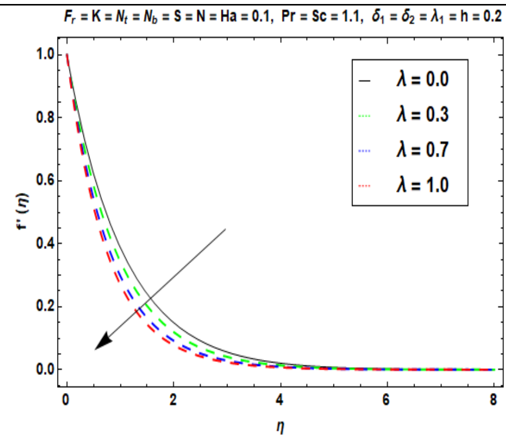

Fig. 5. Impact of $f'(\eta)$ via λ.

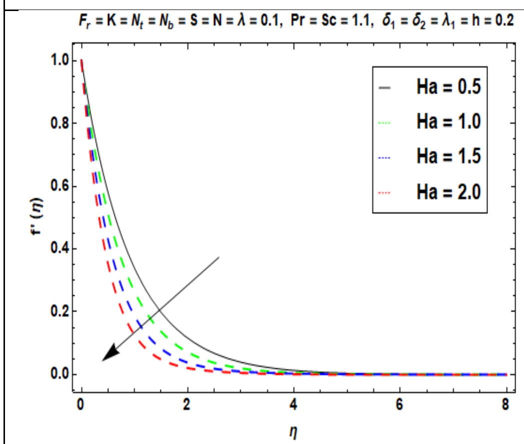

Fig. 6. Impact of $f'(\eta)$ via Ha.

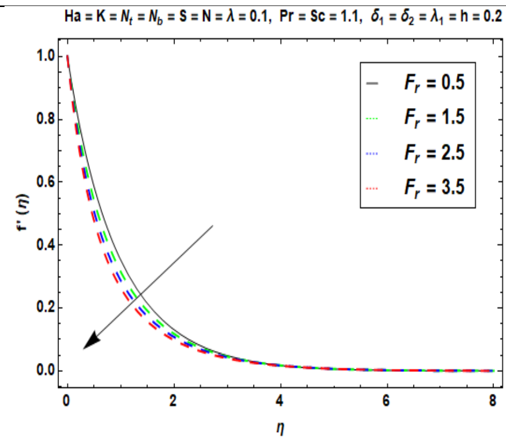

Fig. 7. Impact of $f'(\eta)$ via F_r

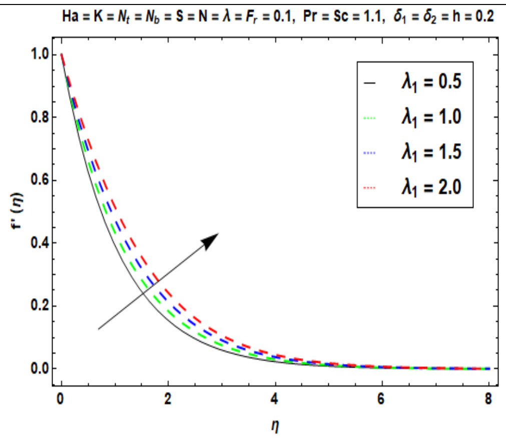

Fig. 8. Impact of $f'(\eta)$ via λ_1

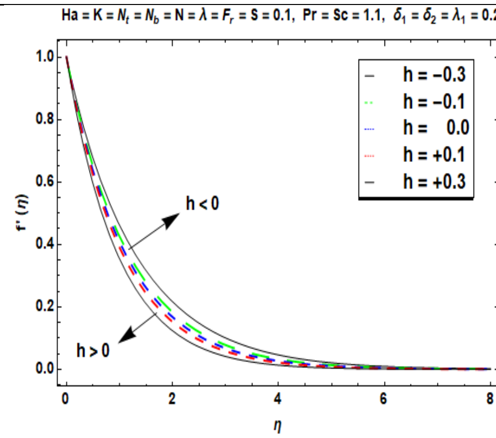

Fig. 9. Impact of $f'(\eta)$ via h.

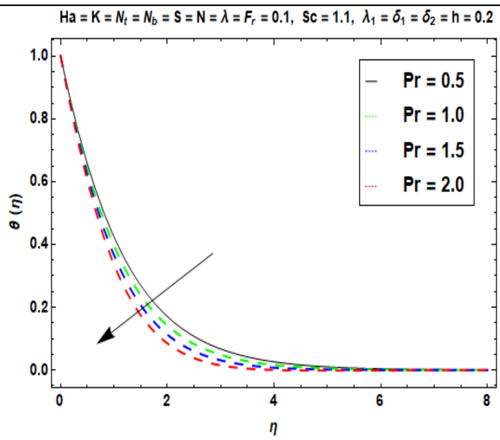

Fig. 10. Impact of $\theta(\eta)$ via Pr.

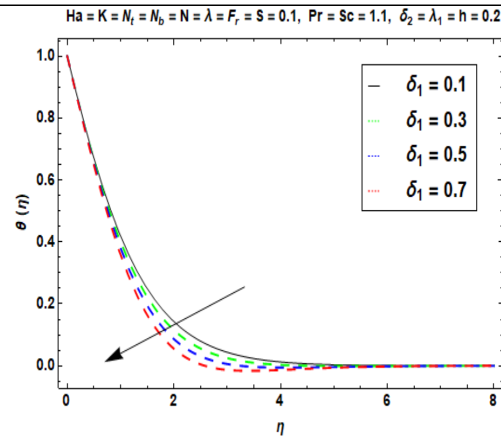

Fig. 11. Impact of $\theta(\eta)$ via δ_1.

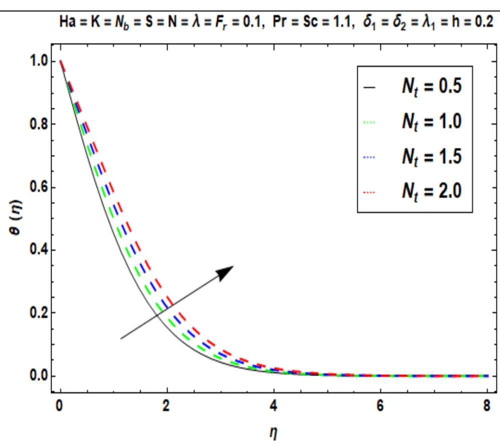

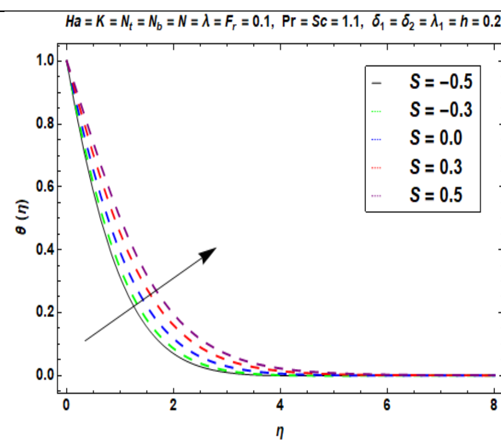

Fig. 12. Impact of $\theta(\eta)$ via N_t.

Fig. 13. Impact of $\theta(\eta)$ via S.

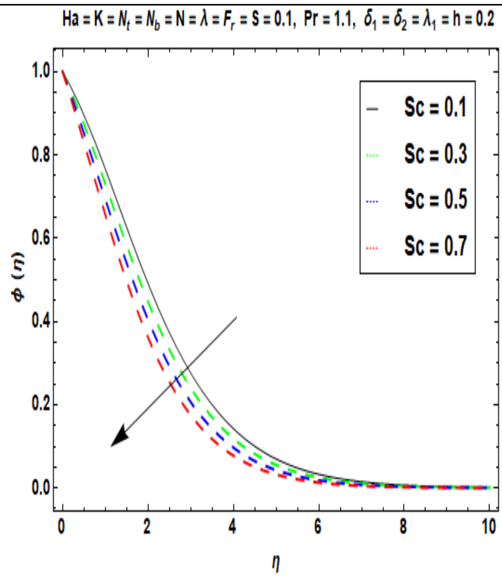

Fig. 14. Impact of $\phi(\eta)$ via Sc.

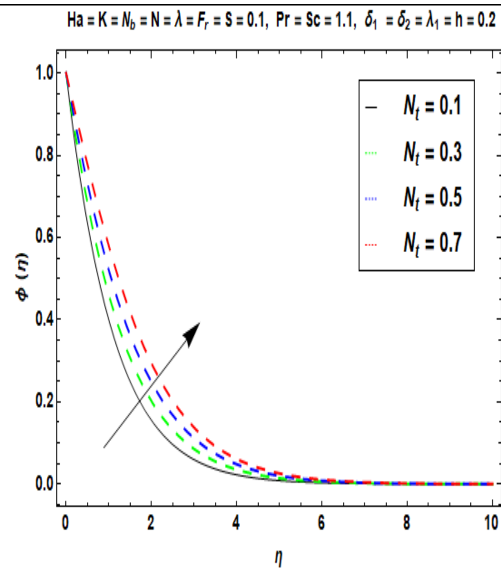

Fig. 15. Impact of $\phi(\eta)$ via N_t.

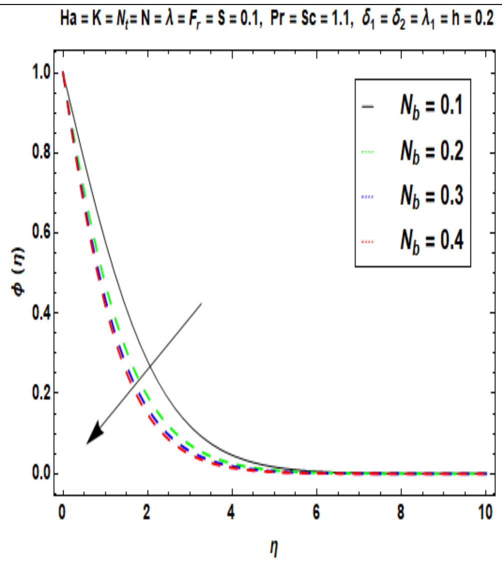

Fig. 16. Impact of $\phi(\eta)$ via N_b.

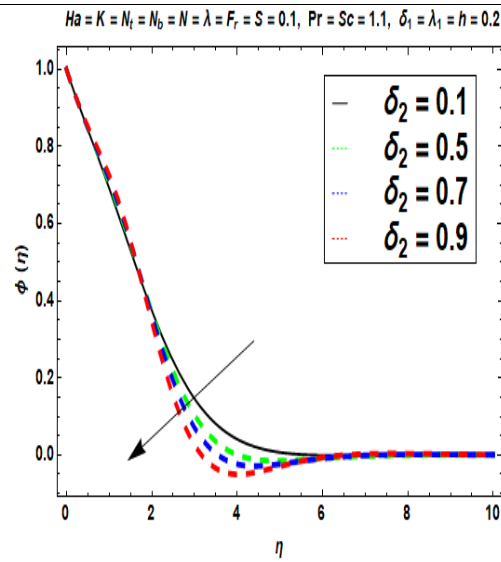

Fig. 17. Impact of $\phi(\eta)$ via δ_2.

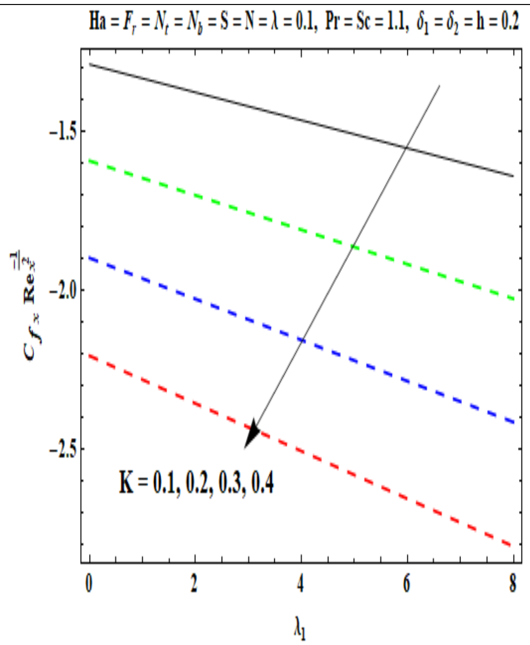

Fig. 18. $Cf_x \mathrm{Re}_x^{\frac{-1}{2}}$ against K.

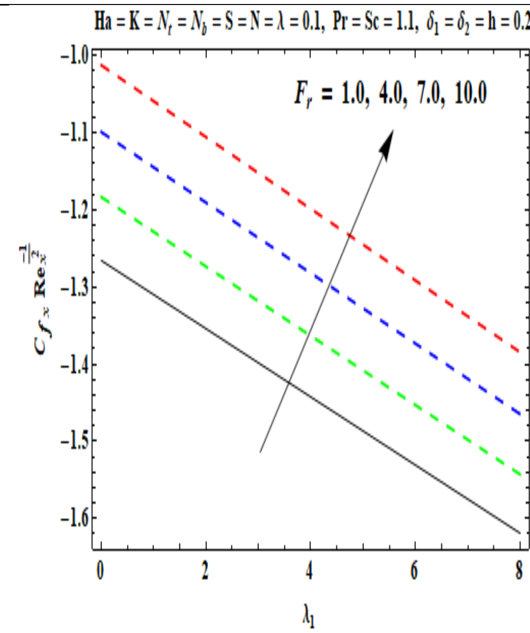

Fig. 19. $Cf_x \mathrm{Re}_x^{\frac{-1}{2}}$ against F_r.

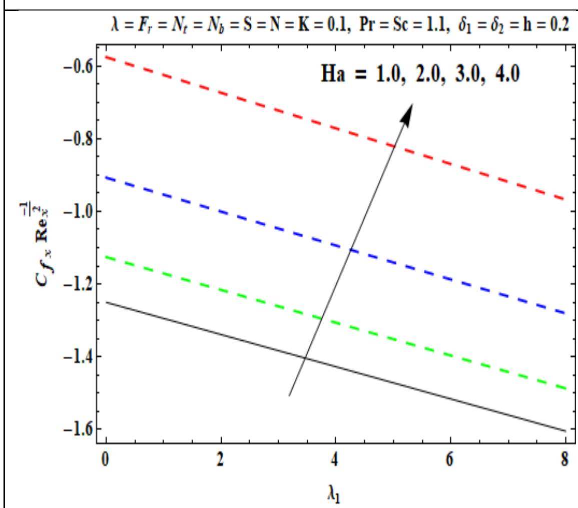

Fig. 20. $Cf_x \mathrm{Re}_x^{\frac{-1}{2}}$ against Ha.

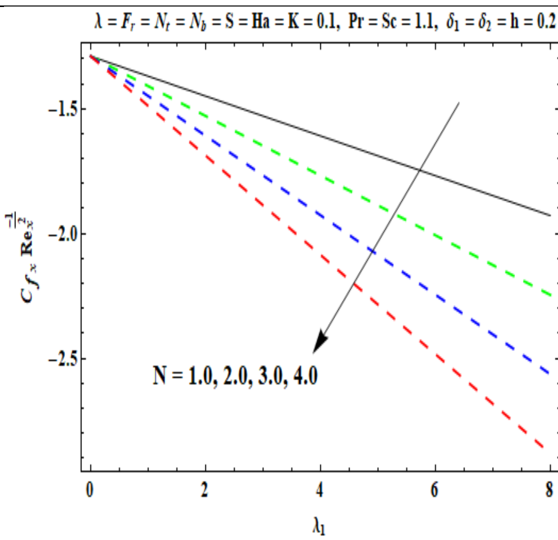

Fig. 21. $Cf_x \mathrm{Re}_x^{\frac{-1}{2}}$ against N.

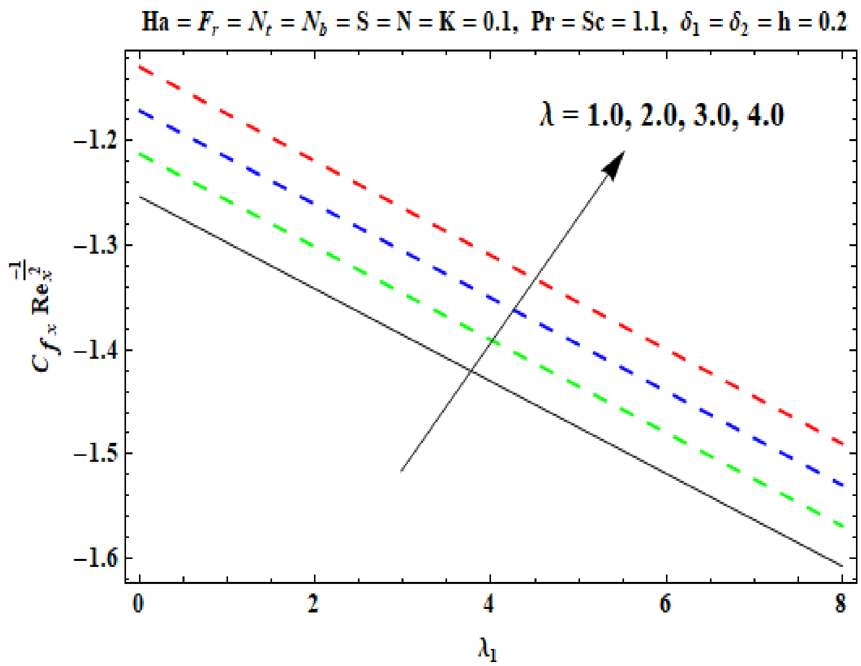

Fig. 22. $Cf_x \mathrm{Re}_x^{\frac{-1}{2}}$ against λ.

In these figures data is extracted to represent as accurately as possible the actual characteristics of industrial flows [12, 13, 18]. The default data prescribed is as follows: $F_r = \lambda = N_t = N_b = S = 0.1, N = Ha = 0.1, \Pr = Sc = 1.1, \delta_1 = \delta_2 = \lambda_1 = h = 0.2$, unless otherwise stated.

Figs. 4–9 the effects of various physical variables on velocity $f'(\eta)$ for different values of selected parameters e.g. viscoelastic second–grade material parameter K, permeability parameter λ, modified Hartmann number Ha, local Forchheimer inertia coefficient F_r, mixed convection parameter λ_1, and suction/injection parameter h are presented. **Fig. 4.** shows that velocity $f'(\eta)$ increases via progressive increment in K. The second order viscoelastic parameter, $K = \frac{\alpha_1 c}{\mu}$ and is inversely proportional to the dynamic viscosity of the magnetic nanopolymer. As K increases viscosity decreases and elastic tensile stresses increase which encourages flow acceleration in the boundary layer. This manifests with a strong elevation in velocity. K arises in the modified shear terms, $+K\left(2f'f''' - f''^2 - ff^{iv}\right)$ in the momentum (velocity) boundary layer Eqn. (8) and clearly exerts a substantial influence on the momentum characteristics. For the Newtonian case, K = 0 and clearly velocity is minimized. In all cases asymptotically smooth distributions (monotonic decays) are computed from the wall to the free stream. Increasing viscoelastic parameter implies greater elastic effects in the nanofluid relative to viscous effects. Momentum boundary layer thickness is strongly reduced with greater values of *K*, since flow acceleration is induced. The inclusion of a non-Newtonian model is therefore demonstrated to produce more realistic results than purely Newtonian models. **Fig. 5.** shows the evolution in velocity field $f'(\eta)$ through the boundary layer transverse to the vertical stretching sheet, with variation in Darcy permeability parameter, $\lambda = \frac{\upsilon}{K^{*}c}$. This parameter appears, as expected, only in the momentum boundary layer Eqn. (8), via the Darcian linear drag (impedance) term, $-(\lambda)f'$ which is clearly negative and resistive. As $-(\lambda + Ha^2)f'$ increases, the permeability decreases, and this increases the Darcian resistance leading to flow deceleration i. e. a decrease in velocity magnitudes. For the case $\lambda = 0$, infinite permeability arises i. e. the porous media fibers vanish and clearly the flow velocity is a maximum. The damping of the velocity field is clearly achieved with lower permeability (greater presence of solid matrix fibers in the porous medium) which is a useful mechanism therefore for flow regulation in materials processing. Momentum boundary layer thickness is therefore increases, with greater values of Darcy parameter, λ . Fig. 6. depicts the response in velocity $f'(\eta)$ to a change in modified magnetic parameter, *Ha*. With increasing values of this parameter, the Lorentzian magnetic drag simulated via the term $-(Ha^2)f'$ in Eqn. (8) is enhanced. This decelerates the flow strongly and increases momentum boundary layer thickness. Strong damping in the flow is therefore achievable with the imposition of a strong transverse magnetic field. This permits the manipulation of smart coating characteristics in magnetic polymer materials synthesis operations [12]. The impact of Forchheimer inertial porous medium drag parameter, F_r on $f'(\eta)$ profiles is illustrated in **Fig. 7.** Increment in Forchheimer parameter induces a strong decrease in $f'(\eta)$, and an associated elevation in momentum boundary layer thickness. Inertial drag therefore has a strong dampening effect on the boundary layer flow. When *Fr = 0* the Darcy case is retrieved and inertial effects are negated. Effectively therefore while the flow percolates in the porous medium at Reynolds numbers above the Darcy limit, the net effect of Forchheimer quadratic drag, $-(1 + F_r)f'^2$ is to decelerate the flow. **Fig. 8.** illustrates the influence of mixed convection parameter, λ_1 on velocity $f'(\eta)$. For this graph, the data prescribed i.e. $Ha = K = N_t = N_b = S = N = \lambda = F_r = 0.1$, $\Pr = Sc = 1.1$, $\delta_1 = \delta_2 = h = 0.2$

implies weak magnetic field and Darcy and Forchheimer impedance are also relatively weak. Distinct from the Darcy, Lorentz magnetic and Forchheimer inertial body forces, the thermal and species buoyancy forces, as simulated via the coupling term, $+\lambda_1(\theta + N\phi)$ in the momentum Eqn. (8) are assistive i. e. they aid in momentum development. Velocity $f'(\eta)$ therefore rises with increment in λ_1 since higher values of λ_1 correspond to the greater thermal buoyancy force (relative to the species buoyancy force) which energizes the boundary layer via thermal convection currents. Momentum (hydrodynamic) boundary layer thickness is therefore decreased with greater mixed convection parameter values. **Fig. 9.** displays the impact of suction/injection parameters on the non–dimensional linear velocity $f'(\eta)$ and in this plot the data prescribed is $Ha = K = N_t = N_b = N = \lambda = F_r = S = 0.1,$ $\Pr = Sc = 1.1,$ $Ha = K = 0.1,$ $\delta_1 = \delta_2 = \lambda_1 = 0.2$. It is noted that with increasing suction $(h > 0)$ decreases, the fluid velocity $f'(\eta)$ is also reduced, since lateral mass flux via the permeable wall out of the boundary layer causes adhesion of the boundary layer to the sheet and destroys momentum. Momentum boundary layer thickness is therefore increased with greater wall suction. On the other hand, the velocity $f'(\eta)$ increases with increment in injection parameter $(h < 0)$, since blowing mass via the wall assist momentum and leads to a thinner momentum boundary layer thickness (flow acceleration).

Figs. 10–13 visualize the impacts of Prandtl number $\Pr$, thermal relaxation variable δ_1, thermophoresis variable N_t and heat generation / absorption parameter S on the temperature $\theta(\eta)$. Increment in $\Pr$ reduces strongly the values of $\theta(\eta)$ as exposed in **Fig. 10**. Data has been extracted from [13]. Thermal boundary layer thickness is therefore also reduced with greater values of $\Pr$. Prandtl number expresses the relative rate of momentum and thermal diffusion. When $Pr = 1$ both momentum and heat diffuse at the same rate. For $Pr > 1$ momentum diffuses faster than heat and vice versa for $\Pr < 1$. With increment in $\Pr$, thermal diffusivity is weaker, and the thermal conductivity is also reduced of the magnetic nanofluid. This decreases the rate of thermal diffusion in the liquid and induces a cooling effect via a decrease in temperatures in the boundary layer. Generally, it is observed that higher $\Pr$ produces lower temperatures throughout the regime whereas lower Pr generates higher temperatures. The influence of non-Fourier thermal relaxation parameter, δ_1 on $\theta(\eta)$ is depicted in Figure 11, for which the data prescribed is $Ha = K = N_t = N_b = N = \lambda = F_r = S = 0.1$, $\Pr = Sc = 1.1, \delta_2 = \lambda_1 = h = 0.2$. It is perceived that the temperature $\theta(\eta)$ is reduced with increasing thermal relaxation δ_1. Thermal boundary layer thickness is therefore decreased. The implication is that a classical Fourier model (for which δ_1 = 0 and therefore the non-Fourier terms, $\boldsymbol{Pr}\, S\, \delta_1 f \theta' + \boldsymbol{Pr}\, \delta_1 \left(-ff'\theta' - f^2\theta'' - 2N_t f\theta'\theta'' - N_b f\theta'\phi'' - N_b f\theta''\phi'\right)$ in Eqn. (9) would vanish) over-predicts the temperatures. To achieve more accurate results the non-Fourier model is required, and temperatures predicted are lower with stronger thermal relaxation effects. Larger relaxation time implies that the liquid needs more time to transport heat to neighboring elements and this delay manifests in temperature decay i. e. $\theta(\eta)$ decay and an associated decrease in thermal boundary layer thickness. **Fig. 12.** exhibits the influence of N_t on $\theta(\eta)$, for $Ha = K = N_b = S = N = \lambda = F_r = 0.1$, $\Pr = Sc = 1.1, \delta_1 = \delta_2 = \lambda_1 = h = 0.2$ are fixed. It is evident that with increment in N_t there is a substantial boost in $\theta(\eta)$. The thermophoresis force is amplified with enhancement in N_t which corresponds to more intensive migration of nanoparticles from the hot zones in the boundary layer to cold zones. This migration of nanoparticles generates thermal energy transfer which heats the regime and increases thermal boundary layer thickness. Fig. 13 shows the influence of the heat source/sink parameter S on $\theta(\eta)$. It should be remarked that with greater values of $S > 0$ (more intense heat generation such as in a hotspot in materials coating), $\theta(\eta)$ and thermal boundary layer upsurge, whereas the reverse effect is induced for $S < 0$ (heat sink in which heat is drained from the coating material and leads to cooling). Clearly it is possible to manipulate temperatures significantly with a heat source/sink. Againm in all Figs. 10-13, smooth distributions are computed in the free stream (all plots are monotonic decays from the wall) and this confirms that an adequately large infinity boundary condition has been used in the homotopy computations.

Figs. 14–17 visualize the effects of Schmidt number Sc, thermophoresis variable N_t, Brownian motion variable N_b and concentration (non-Fickian solutal) relaxation factor δ_2 on nanoparticles species concentration, $\phi(\eta)$. The impact of Sc verses $\phi(\eta)$ is exhibited in **Fig**

14. Here $\phi(\eta)$ decreases for greater values of Sc (the other parameters are prescribed as $Ha = K = N_t = N_b = N = \lambda = F_r = S = 0.1,\ \Pr = 1.1, \delta_1 = \delta_2 = \lambda_1 = h = 0.2$). Schmidt number expresses the relative rate of momentum diffusion and species (nanoparticle) diffusion. It also embodies the ratio of velocity and species boundary layer thicknesses. Data is extracted from [13] to represent actual species diffusion in viscoelastic nanofluids in materials processing. Physically, an increment in Sc corresponds to a reduction in molecular diffusivity of the nanoparticles- this results in a decline in magnitudes of concentration, $\phi(\eta)$. Concentration boundary layer thickness is therefore also reduced. **Figs. 15 and 16** illustrate the impact of N_t and N_b stimulus on $\phi(\eta)$. When N_t is increased, an enhancement is seen in $\phi(\eta)$, while opposite trend is seen for N_b. Greater thermophoretic body force encourages migration of nanoparticles from the hot regions to the colder regions under a temperature gradient. This enhances species diffusion and elevates concentration boundary layer thickness (Fig. 15). However greater Brownian motion relates to the intensification in ballistic collisions of nanoparticles due to a reduction in the size of nanoparticles [14]. Species diffusion is therefore inhibited with greater random motion and the concentration boundary layer thickness is reduced. These trends have been confirmed in numerous other studies including [15], [18] and [19] i. e. the influence of thermophoresis and Brownian motion are *opposite* on the nanoparticle species concentration field. The evolution in concentration, $\phi(\eta)$ with non-Fickian concentration relaxation variable δ_2 are captured in **Figs. 17**. An enhancement in δ_2 produce smaller $\phi(\eta)$ with fixed values of all other physical parameters $Ha = K = N_t = N_b = N = \lambda = F_r = S = 0.1,\ \Pr = Sc = 1.1, \delta_1 = \lambda_1 = h = 0.2$. This is particularly pronounced at intermediate distances from the wall (stretching sheet). A delay in the diffusion of nanoparticle species is incurred with greater solutal relaxation effect. This produces lower values of concentration compared with the conventional Fickian species diffusion model which over-predicts concentration magnitudes. Concentration boundary layer thickness is therefore also depleted with increasing solutal relaxation effect. Again, similar observations have been reported in many other studies including [31] and [32], confirming the validity of the present homotopy simulations.

Finally, **Figs. 18–22** illustrate the variation of wall skin friction coefficient (dimensionless shear stress at the permeable stretching sheet surface) i.e. $C_{fx}\,\mathrm{Re}_x^{-\frac{1}{2}} = (1+3K)\,f''(0)$, plotted against mixed convection parameter, $\lambda_1 = \frac{Gr_x}{\boldsymbol{Re_x^2}}$ for some selected parameters. Magnitude of skin friction coefficient is elevated with increase in local inertia coefficient F_r (Fig. 19), enhanced with greater magnetic number, Ha (Fig. 20) and also greatly boosted with increase in Darcy permeability parameter (Fig. 22). However, skin friction coefficient is strongly reduced with increment in viscoelastic material parameter K (Fig. 18) and also ratio of concentration to thermal buoyancy force, N .

5. CONCLUSIONS

Inspired by novel developments in electroconductive polymeric coating flows, in the present article, a novel mathematical model has been developed for *mixed convection hydromagnetic flow of electrically conducting viscoelastic nanofluid from a vertical permeable stretching sheet in a non-Darcy porous medium with the Cattaneo–Christov double diffusion model (thermal and solutal relaxation effects).* Heat absorption/generation has been included and the Buongiorno two-component nanoscale model employed. A Darcy-Forchheimer drag force model has been implemented for the porous medium and the Reiner-Rivlin differential second grade model for non-Newtonian characteristics (relaxation and retardation). The novelty of the work is the simultaneous inclusion of all these multiple effects which are relevant to rheological nanomaterials processing and also the deployment of homotopy analysis as an alternative to conventional numerical methods such as finite differences, finite elements and MATLAB solvers. Via appropriate dimensionless similarity variables, the non–linear dimensional partial differential conservation equations for momentum, energy and concentration with associated boundary conditions have been transformed into a non–linear dimensionless ordinary differential boundary value problem. The homotopy analysis method (HAM) has been employed to solve the boundary value problem. The main findings of the present analysis may be summarized as follows:

(i) Velocity $f'(\eta)$ is elevated (and momentum boundary layer thickness decreased) with increasing mixed convection parameter λ_1 whereas velocity is depleted (and momentum boundary layer thickness is increased) with greater Darcy permeability parameter λ .

(ii) Velocity $f'(\eta)$ is boosted (and momentum boundary layer thickness depleted) with greater second order viscoelastic (non-Newtonian) parameter K whereas velocity is decreased (and momentum boundary layer thickness is elevated) with increment in the Forchheimer inertial drag parameter, F_r.

(iii) The wall temperature $\theta(\eta)$ and thermal boundary layer thickness are reduced with increasing non-Fourier thermal relaxation parameter, δ_1.

(iv) Temperature $\theta(\eta)$ is enhanced (as is thermal boundary layer thickness) with greater heat generation ($S > 0$) whereas the converse effects are computed with greater heat absorption ($S < 0$).

(v) Nanoparticle concentration $\phi(\eta)$ is elevated as is species boundary layer thickness with increment in thermophoresis parameter (N_t) whereas the opposite behaviour is observed with an increment in Brownian motion parameter (N_b).

(vi) Nanoparticle concentration $\phi(\eta)$ and species boundary layer thickness are decreased with greater values of non-Fickian solutal relaxation parameter, δ_2.

(vii) Magnitude of skin friction coefficient is boosted with increase in local inertia coefficient F_r, magnetic number, Ha and Darcy permeability parameter.

(viii) Skin friction coefficient is strongly depleted with increment in viscoelastic material parameter K and also ratio of concentration to thermal buoyancy force, N.

(ix) Homotopy analysis method (HAM) provides an excellent semi-numerical approach for studying nonlinear magnetic nanopolymer coating flows.

The present study has ignored magnetic induction effects which arise at higher values of magnetic Reynolds number. These may be considered in future simulations [39]. Furthermore, alternative non-Newtonian nanofluid formulations may be examined including Williamson nanofluids [40], Carreau nanofluids [41] and Stokes polar couple stress nanofluids [42, 43] these will be explored imminently.

REFERENCES

1] Grattan-Guinness, I. (2005). Joseph Fourier, *Théorie analytique de la chaleur* (1822). In *Landmark Writings in Western Mathematics 1640-1940* (pp. 354-365). Elsevier Science.

2] Cattaneo, C. (1948). Sulla conduzione del calore. *Atti Sem. Mat. Fis. Univ. Modena*, *3*, 83-101.

3] Christov, C. I. (2009). On frame indifferent formulation of the Maxwell–Cattaneo model of finite-speed heat conduction. *Mechanics Research Communications*, *36*(4), 481-486.

4] Straughan, B. (2010). Thermal convection with the Cattaneo–Christov model. *International Journal of Heat and Mass Transfer, 53*(1-3), 95-98.

5] Hayat, T., Qayyum, S., Shehzad, S. A., & Alsaedi, A. (2017). Chemical reaction and heat generation/absorption aspects in flow of Walters-B nanofluid with Cattaneo-Christov double-diffusion. *Results in physics*, *7*, 4145-4152.

6] Hayat, T., Qayyum, S., Shehzad, S. A., & Alsaedi, A. (2018). Cattaneo-Christov double-diffusion theory for three-dimensional flow of viscoelastic nanofluid with the effect of heat generation/absorption. *Results in Physics*, *8*, 489-495.

7] Bai, Y., Xie, B., Zhang, Y., Cao, Y., & Shen, Y. (2019). Stagnation-point flow and heat transfer of upper-convected Oldroyd-B MHD nanofluid with Cattaneo–Christov double-diffusion model. *International Journal of Numerical Methods for Heat & Fluid Flow*.

8] Ijaz, M., & Ayub, M. (2019). Activation energy and dual stratification effects for Walter-B fluid flow in view of Cattaneo-Christov double diffusion. Heliyon, 5(6), e01815.

9] Ibrahim, W., & Gadisa, G. (2020). Finite element solution of non-linear convective flow of Oldroyd-B fluid with Cattaneo-Christov heat flux model over non-linear stretching sheet with heat generation or absorption. *Propulsion and Power Research*, *9*(3), 304-315.

10] Tulu, A., & Ibrahim, W. (2020). Spectral relaxation method analysis of Casson nanofluid flow over stretching cylinder with variable thermal conductivity and Cattaneo–Christov heat flux model. *Heat Transfer*, *49*(6), 3433-3455.

11] Rawat, S. K., Upreti, H., & Kumar, M. (2021). Numerical study of activation energy and thermal radiation effects on Oldroyd-B nanofluid flow using the Cattaneo–Christov double diffusion model over a convectively heated stretching sheet. *Heat Transfer*.

12] Kung-Chin Chang and Jui-MingYeh, Chapter 16 - Electroactive Polymer-Based Anticorrosive Coatings, in *Intelligent Coatings for Corrosion Control, Eds. Atul Tiwari, James Rawlins and Lloyd H. Hihara*, 557-583, Butterworth-Heinemann, USA (2014).

13] Murr L.E. Synthesis and Processing of Nanomaterials. In: *Handbook of Materials Structures*, *Properties*, *Processing and Performance*. Springer, USA (2015).

14] Buongiorno J., Convective transport in nanofluids, *ASME J Heat Trans.*, Vol. 128, Issue 3, 240-250, (2006).

15] G. Kumaran, R Sivaraj, V. Ramachandra Prasad, O. Anwar Bég, Numerical study of axisymmetric magneto-gyrotactic bioconvection in non-Fourier tangent hyperbolic nano-functional reactive coating flow of a cylindrical body in porous media, *European Physical Journal Plus, 136, 1107 (2021).* *https://doi.org/10.1140/epjp/s13360-021-02099-z (32 pages)*

16] J.C. Umavathi, S.L. Patil, B. Mahanthesh and O. Anwar Bég, Unsteady squeezing flow of magnetized nano-lubricant between parallel disks with Robin boundary condition, *Proc. IMechE J. Nanomaterials, Nanoengineering and Nanosystems (2020). DOI: 10.1177/23977914211036562 (15 pages)*

17] M. Ali Abbas, O. Anwar Bég, A. Zeeshan, A. Hobiny, M. M. Bhatti, Parametric analysis and minimization of entropy generation in bioinspired magnetized non-Newtonian nanofluid pumping using artificial neural networks and particle swarm optimization, *Thermal Science and Engineering Progress (2021). doi.org/10.1016/j.tsep.2021.100930 (10 pages)*

18] Hayat, T., Shah, F., & Alseadi, A. (2020). Cattaneo-Christov double diffusions and entropy generation in MHD second grade nanofluid flow by a Riga wall. *International Communications in Heat and Mass Transfer, 119*, 104824

19] Hafeez, A., Khan, M., Ahmed, A., & Ahmed, J. (2020). Rotational flow of Oldroyd-B nanofluid subject to Cattaneo-Christov double diffusion theory. *Applied Mathematics and Mechanics*, *41*, 1083-1094.

20] Ijaz, M., Yousaf, M., & El Shafey, A. M. (2021). Arrhenius activation energy and Joule heating for Walter-B fluid with Cattaneo–Christov double-diffusion model. *Journal of Thermal Analysis and Calorimetry*, *143*(5), 3687-3698.

21] Ismail A.K., Abdullah M.Z., Jamaludin A.R., Zubair M., Ibrahim N.H. (2019) *Flow Analysis Inside Coated Porous Media. In: Ismail A., Abu Bakar M., Öchsner A. (eds) Advanced Engineering for Processes and Technologies. Advanced Structured Materials*, vol 102. Springer, China. https://doi.org/10.1007/978-3-030-05621-6_13

22] X. Ding et al., Review on penetration and transport phenomena in porous media during slot die coating, *J. Polym. Sci., Part B: Polym. Phys*. 2017, *55*, 1669–1680 (2017).

23] MD. Shamshuddin, S.R. Mishra, O. Anwar Bég, T.A. Bég and Ali Kadir, Computation of radiative Marangoni (thermocapillary) magnetohydrodynamic convection in Cu-water based nanofluid flow from a disk in porous media: smart coating simulation, *Heat Transfer (2020). DOI: 10.1002/htj.21963 (20 pages)*

24] M.M. Bhatti, C.M. Khalique, Tasveer Bég, O. Anwar Bég and Ali Kadir, Numerical study of slip and radiative effects on magnetic Fe_3O_4-water-based nanofluid flow from a nonlinear stretching sheet in porous media with Soret and Dufour diffusion, *Modern Physics Letters B 33, 2050026 (24 pages) (2020).*

25] M. Shamshuddin, S.R. Mishra, O. Anwar Bég and Ali Kadir, Adomian computation of radiative-convective stretching flow of a magnetic non-Newtonian fluid in a porous medium with homogeneous–heterogeneous reactions, *Int. J Modern Physics B, 33 (2) (2020).* (28 pages).

26] Ashis Kumar Roy, O. Anwar Bég, Apu Kumar Saha and J. V. Ramana Murthy, Taylor dispersion in non-Darcy porous media with bulk chemical reaction: a model for drug transport in impeded blood vessels, *J. Engineering Mathematics, 127:24 (18 pages) (2021).*

27] A. Shahid, M. M. Bhatti, O. Anwar Bég, I. L. Animasaun and K. Javid, Spectral computation of reactive bi-directional hydromagnetic non-Newtonian convection flow from a stretching upper parabolic surface in non-Darcy porous medium, *Int. J. Modern Physics B (2021). 2150294 (26 pages).* DOI: 10.1142/S0217979221502945

28] Revathi, G., Saikrishnan, P., Revathy, M., & Jayanthi, S. (2020). Numerical study of Darcy Forchheimer unsteady mixed convection flow of nanofluid with an exponentially decreasing free-stream velocity distribution. *Computational Thermal Sciences: An International Journal*, *12*(4).

29] Khan, M. I., & Alzahrani, F. (2021). Dynamics of activation energy and non-linear mixed convection in Darcy-Forchheimer radiated flow of Carreau nanofluid near stagnation point region. *Journal of Thermal Science and Engineering Applications*, *13*(5), 051009.

30] Umavathi, J. C., Buonomo, B., Manca, O., & Sheremet, M. A. (2021). Heat transfer of chemically reacting mixed convection fluid using convective surface condition: Non-Darcy model. *Thermal Science and Engineering Progress*, 101044.

31] Muhammad, T., Rafique, K., Asma, M., & Alghamdi, M. (2020). Darcy–Forchheimer flow over an exponentially stretching curved surface with Cattaneo–Christov double diffusion. *Physica A: Statistical Mechanics and its Applications*, *556*, 123968.

32] Nayak, M. K., Shaw, S., Waqas, H., & Muhammad, T. (2021). Numerical computation for entropy generation in Darcy-Forchheimer transport of hybrid nanofluids with Cattaneo-Christov double-diffusion. *International Journal of Numerical Methods for Heat & Fluid Flow*.

33] Liao, S. (2012). *Homotopy analysis method in non-linear differential equations* (pp. 153-165). Beijing: Higher education press, China.

34] O. Anwar Bég, Tasveer A. Bég, S.R. Munjam and S. Jangili, Homotopy and Adomian semi-numericalsolutions for oscillatory flow of partially ionized dielectric hydrogen gas in a rotating MHD energy generator duct, *Int. J. Hydrogen Energy*, 46, 17677-17696 (2021).

35] O. Anwar Bég, B. Vasu, Atul Kumar Ray, T.A. Bég, Ali Kadir, Henry J. Leonard and R.S.R. Gorla, Homotopy simulation of dissipative micropolar flow and heat transfer from a two-dimensional body with heat sink effect: applications in polymer coating, *Chem. Biochem. Eng. Quart.* 34 (4) 257–275 (2020).

36] O. Anwar Bég, Tasveer A. Bég, M. Ferdows, B. Vasu, Ali Kadir, H. J. Leonard and S. Kuharat, Unsteady nonlinear magnetohydrodynamic micropolar transport phenomena with Hall and ion-slip current effects: numerical study, *Int. J. Applied Electromagnetics & Mechanics,* 1-33 (2020). *DOI 10.3233/JAE-201508 (33 pages)*

37] N. Shukla, P. Rana, O. Anwar Bég, Bani Singh and A. Kadir, Homotopy study of magnetohydrodynamic mixed convection nanofluid multiple slip flow and heat transfer from a vertical cylinder with entropy generation, *Propulsion and Power Research* (2019). *https://doi.org/10.1016/j.jppr.2019.01.005 (16 pages)*

38] J. Srinivas and O. Anwar Bég, Homotopy study of entropy generation in magnetized micropolar flow in a vertical parallel plate channel with buoyancy effect, *Heat Transfer Research*, 49(6): 529–553 (2018).

39] O. Anwar Bég, S. Kuharat, M. Ferdows, M. Das, A. Kadir, M. Shamshuddin, Magnetic nano-polymer flow with magnetic induction and nanoparticle solid volume fraction effects: *solar magnetic nano-polymer fabrication simulation, Proc. IMechE-Part N: J Nanoengineering, Nanomaterials and Nano-systems (2019).* DOI: 10.1177/ 2397791419838714 (19 pages)

40] H. Thameem Basha *et al.*, Impacts of temperature dependent viscosity and variable Prandtl number on forced convective Falkner–Skan flow of Williamson nanofluid, *SN Applied Sciences* volume 2, Article number: 477 (2020).

41] G. Kumaran *et al.*, Hydromagnetic forced convective flow of Carreau nanofluid over a wedge/plate/ stagnation of the plate, *The European Physical Journal Special Topics* volume 228, pages2647–2659 (2019).

[42] G.J. Reddy et al., Study of entropy generation in transient hydromagnetic flow of couple stress fluid due to heat and mass transfer from a radiative vertical cylinder, Pramana – Journal of Physics. **volume 93**, Article number: 103 (2019).

[43] R. Ravi et al., Study of Soret and Dufour effects and secondary instabilities on Rayleigh-Benard convection in a couple stress fluid, The European Physical Journal Plus, **volume 133**, Article number: 513 (2018).